International Journal of Fatigue 115 (2018) 67–78

Contents lists available at ScienceDirect

International Journal of Fatigue

journal homepage: www.elsevier.com/locate/ijfatigue

The behavior of crack initiation and early growth in high-cycle and very-high-cycle fatigue regimes for a titanium alloy

Xiangnan Pan, Hang Su, Chengqi Sun, Youshi Hong*

State Key Laboratory of Nonlinear Mechanics, Institute of Mechanics, Chinese Academy of Sciences, Beijing 100190, China
School of Engineering Science, University of Chinese Academy of Sciences, Beijing 100049, China

ARTICLE INFO

Keywords:
Very-high-cycle fatigue
Crack initiation
Mean stress
Titanium alloy
Equiaxed microstructure

ABSTRACT

The behavior of crack initiation and early growth in high-cycle fatigue (HCF) and very-high-cycle fatigue (VHCF) regimes for a TC4 titanium alloy with equiaxed microstructure was investigated. Fatigue tests were conducted via ultrasonic axial cycling (20 kHz) superimposed by an amount of tensile load. The effect of tensile mean stress on fatigue endurance was plotted with a Haigh diagram formulated by Goodman, Gerber and the present formula. Fractography was observed by scanning electron microscopy, and three failure types of crack initiation were classified: surface-without-RA (rough area), surface-with-RA and interior-with-RA. Profile samples from the crack initiation region were prepared and examined by transmission electron microscopy with selected area electron diffraction. The observations show that a nanograin layer prevails underneath the fracture surface in the RA region only for the VHCF case with a stress ratio $R = -1$. The nanograin formation mechanism was explained by the numerous cyclic pressing (NCP) model.

1. Introduction

Titanium alloys have been widely used as superior structural and functional materials in many engineering applications due to their high specific strength, high temperature resistance and high corrosion resistance. Fatigue damage is one of the key failure issues for engineering components and structures. Based on the requirement of having safe performance for 10^7 or more loading cycles, the very-high-cycle fatigue (VHCF) behavior of metallic materials has drawn increased attention [1–4]. The mechanism of fatigue crack initiation and early growth is still a crucial issue for investigation, although fatigue crack growth (FCG) can be empirically assessed by the Paris equation. In particular, understanding this mechanism is of great importance in the VHCF regime because more than 95% of the total fatigue life is consumed in the crack initiation stage [5–7].

In the early 1980s, Naito et al. [8,9] studied the fatigue behavior up to 10^8 cycles of fatigue life for carburized steels, showing fatigue strength decreasing with loading cycle without an endurance limit and crack initiation at the subsurface with a typical fractographic feature of fish eye (FiE) for the specimens that failed beyond 5×10^6 cycles. Atrens et al. [10] reported similar phenomena in a titanium alloy (Ti-6Al-4V).

With respect to crack initiation from the surface or from the interior of a specimen, there is a tendency for S-N curves to have a twofold or stepwise shape for high-strength steels [11,12]. Fatigue crack initiation at the interior of the specimen always originated from relevant inhomogeneity, usually an inclusion [13,14], due to localized plastic deformation constraints and stress concentrations [4,15]. For the internal crack initiation of VHCF, a rough region around the inclusion was observed and called the fine granular area (FGA) [12]. FiE and FGA are both typical fractographic features for crack initiation and early growth of high-strength steels during the VHCF process. Stanzl-Tschegg et al. [16,17] estimated and compared near threshold FCG with internal cracks of high-strength steels, and the results demonstrated that the FCG rate within FiE is slower than 10^{-10} m/cycle, whereas the FCG rate outside the FiE region is faster than 10^{-9} m/cycle. The crack growth rate in the FGA region was estimated to be between 10^{-12} m/cycle and 10^{-13} m/cycle in the VHCF regime for high-strength steels [6,16,17]. The summary by Zhao et al. [18] showed that the range of the stress intensity factor (SIF) at the periphery of FGA is close to the FCG threshold for long cracks. Eventually, FGA and FiE were regarded as characteristic regions for internal crack initiation and early growth of high-strength steels in the VHCF regime [6]. The tendency of S-N curves for titanium alloys is different from the shape for high-strength steels due to their distinct microstructures. Although fatigue fracture of titanium alloys can still be induced by surface or internal crack initiation, the dominant mechanisms always differ. Essentially, titanium alloys are almost free of inhomogeneities such as inclusions and micro voids. A

* Corresponding author at: Institute of Mechanics, Chinese Academy of Sciences, Beijing 100190, China.
E-mail address: hongys@imech.ac.cn (Y. Hong).

https://doi.org/10.1016/j.ijfatigue.2018.03.021
Received 29 October 2017; Received in revised form 12 March 2018; Accepted 18 March 2018
Available online 19 March 2018
0142-1123/ © 2018 Elsevier Ltd. All rights reserved.

titanium alloy may appear as one of four typical microstructures, namely equiaxed, bimodal, lamellar or basket weave, or as their mixture, and the microstructure appearance depends on the volume fraction and the shape of the basic phases α and β, with the α phase being a hexagonal close-packed (HCP) crystal structure and the β phase being a body-centered cubic (BCC) structure. The α phase is brittle under cyclic loading [19], and fatigue cracks always initiate from the cleavage of the α phase with facet morphology [20,21]. Zuo et al. [22] studied the effect of microstructure on the VHCF behavior of Ti-6Al-4V and concluded that cracks initiated at the grain boundary and inside the equiaxed α grains (EGs) in the bimodal microstructure (BM). Based on their experimental observations, Liu et al. [23,24] classified three failure types, "surface-without-facets", "surface-with-facets" and "interior-with-facets" in Ti-6Al-4V with BM. Heinz et al. [25,26] showed that the internal fatigue crack initiation site is of FiE morphology, and an FGA-like rough region named rough area (RA) is inside the FiE. Takeuchi et al. [27,28] reported a similar phenomenon in high-cycle fatigue (HCF) and VHCF processes of Ti-6Al-4V with BM, but in some other cases, no clear FiE morphology was observed in the specimens for which cracks also initiated at the interior of the specimen in the VHCF regime. Oguma et al. [29,30] discussed the effects of microstructure and environment on RA formation by introducing the cold-welding model to explain the formation process of the RA region in titanium alloys, although the model was almost a hypothesis. It is noted that the equiaxed microstructure (EM) is very common for titanium alloys, but the fatigue behavior for titanium alloys with EM in the HCF and VHCF regimes is still rarely investigated. The essential characteristics of crack initiation and early growth in the HCF and VHCF regimes for titanium alloys with EM are still unclear and require further investigation.

Recently, Hong et al. [3] overviewed the nature and the mechanism of crack initiation and early growth for metallic materials in VHCF regimes, in which two essential aspects were addressed: what is the nature and what is the mechanism of the fatigue crack initiation region? For high-strength steels, these questions are almost answered. However, for titanium alloys, the microscopic feature of the crack initiation region, i.e., the RA region, should be clearly determined.

With regard to FGA formation, Hong et al. [31] recently revealed that the FGA region of crack initiation in high-strength steels for VHCF is a layer of nanograins on both sides of fracture surfaces, which are formed by numerous cyclic pressing (NCP) at the crack wake. For titanium alloys, Su et al. [32] characterized the RA and FiE regions of the internal fractured specimens in the VHCF regime at stress ratios $R = -1$ and $R = 0.5$ for a Ti-6Al-4V alloy with BM. The observations indicated that nanograin layers formed only in the RA region of crack initiation for the VHCF case under a negative stress ratio ($R < 0$). Hong et al. [3,31] explained this phenomenon by proposing the NCP model and schematically depicted the entire VHCF process from internal crack initiation to final fracture. Even so, the case of titanium alloys with EM still remains to be characterized.

The environmental conditions for HCF and VHCF have also been studied by researchers [33–38]. In particular, Spriestersbach et al. [39] reported that the FGA morphology with nanograins only formed in a vacuum environment. Other investigations [16,17,30,40] have also argued that a vacuum-like environment is a key factor for FGA or RA formation in VHCF of metallic materials. For titanium alloys, it is not clear that if the RA morphology, as well as FiE, only forms under vacuum.

The mean stress σ_m or stress ratio R has an important effect on the fatigue behavior of materials, and many empirical models have been proposed to describe this effect [41–44]. Nevertheless, how the mean stress affects the VHCF behavior of titanium alloys with EM still lacks investigation.

In this paper, a titanium alloy with EM was used to investigate the essential characteristics and the mechanism of crack initiation and early growth in the HCF and VHCF regimes via ultrasonic fatigue testing with tensile mean stress. The fatigue test results were presented as Haigh diagrams, and a formula based on the mechanical properties of the test material was proposed and compared with Goodman and Gerber curves to describe the effect of tensile mean stress on fatigue endurance. The fractographic features of fatigue crack initiation for the specimens that failed in the HCF and VHCF regimes were observed and classified using scanning electron microscopy (SEM). It was observed that cracks initiated from the surface of the specimen under $\sigma_m = 0$ with the RA morphology in the HCF and VHCF regimes. Fatigue crack initiation from the surface shifted to the interior of the specimen with increasing tensile mean stress, and this internal crack initiation was accompanied by the RA morphology in the VHCF regime. Transmission electron microscopy (TEM) samples from different locations within the characteristic RA region of the specimens that failed in the VHCF regime with different stress ratios were prepared by focused ion beam (FIB) milling. The microstructure features underneath the crack initiation region were examined by TEM with bright field imaging (BFI), dark field imaging (DFI) and selected area electron diffraction (SAD). These results were incorporated to reveal the crack initiation mechanism and to discuss the effects of tensile mean stress on the VHCF behavior of the titanium alloy with EM.

2. Test material and methods

2.1. Material

The material tested in this study is an α + β titanium alloy TC4 or Ti-6Al-4V, and the chemical composition is listed in Table 1. Fig. 1 is an SEM image showing the microstructure of the tested material, which is homogeneous EM. As shown in Fig. 1, island-like transformed β is randomly distributed in the EG matrix to provide high mechanical performance. The tensile properties of the material were obtained by a quasi-static (strain rate $10^{-4}\,s^{-1}$) tension test with three cylindrical specimens 10 mm in diameter, which gave the results of yield strength $\sigma_y = 900$ MPa, ultimate tensile strength (UTS) $\sigma_u = 980$ MPa and uniform elongation rate $\delta = 8.25\%$.

2.2. Ultrasonic fatigue test

Ultrasonic fatigue testing method was used in this investigation, which requires that the resonant frequency of the specimen be equal to the input incitation frequency (20 k ± 500 Hz) of the ultrasonic piezoelectric ceramic resonator [45–47]. Fig. 2a shows the shape and dimensions of the ultrasonic fatigue testing specimen, which fulfills the requirement for the generation of the resonant frequency. The specimen has an hourglass shape with a reduced section of 3.5 mm in diameter, for which the stress concentration factor is 1.03. Such specimens were machined from unidirectional rolled round bars 16 mm in diameter of an annealed TC4 alloy with EM.

An ultrasonic fatigue testing machine (Lasur GF20-TC) was equipped with a conventional tensile testing machine (capacity 20 kN) to enable ultrasonic axial cycling superimposed by an amount of tensile force, as shown in Fig. 2. Two amplifying horns were extended to the two ends of the specimen fixed by two screws. One horn was connected to the piezoelectric transducer of the ultrasonic testing machine, and this horn was also installed with the fixture connecting to the crosshead of the tensile testing machine. The other horn was free at $\sigma_m = 0$ or was fixed on the fixture of the tensile machine at $\sigma_m > 0$. When $\sigma_m > 0$, the specimen was subjected to an amount of mean stress by the tensile machine, and the whole specimen system still satisfied the resonant

Table 1
Chemical composition (wt.%) of the tested TC4.

Ti	Al	V	Fe	C	N	H	O
Bal	5.96	4.13	0.16	0.02	0.015	0.0036	0.18

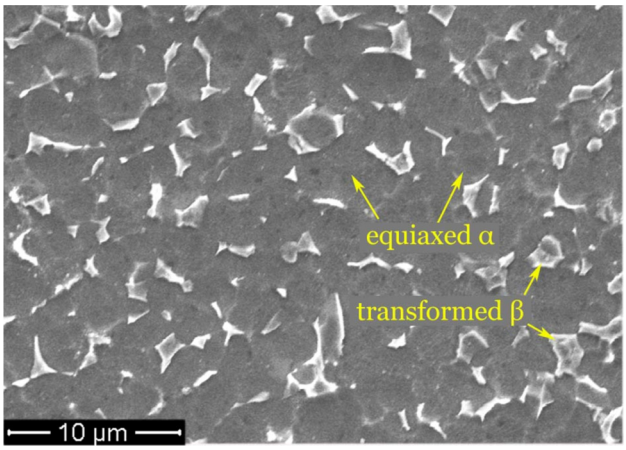

Fig. 1. SEM image of the tested titanium alloy (TC4) showing the equiaxed microstructure (EM).

frequency condition [45–47]. The fatigue tests were conducted at room temperature and in ambient air. The fatigue loading was controlled by displacement in both ultrasonic cycling and tensile loading with the conditions of $\sigma_m = 0$, $\sigma_m = 160$ MPa, $\sigma_m = 440$ MPa, $\sigma_m = 620$ MPa and $\sigma_m = 780$ MPa. In terms of the stress ratio, the fatigue tests were performed in the range from $R = -1$ to $R = 0.8$.

During fatigue testing, the accumulated damage of a specimen will reduce its intrinsic resonant frequency due to crack initiation and propagation. When the resonant frequency is lower than 19.5 kHz, the damaged specimen no longer fulfills the resonant frequency condition, and the ultrasonic vibration stops, which means the termination of the fatigue test with the failure of the specimen.

2.3. Observation methods for the fracture surface and its profile

For the fatigue fractured specimens, optical microscopy (OM) and SEM were employed to examine the fractographic features. SEM observation was carried out especially in the crack initiation region of fracture surfaces using a JEOL JSM-IT300, an FEI Quanta 200 FEG and an FEI Helios Nanolab 600i.

Three specimens that failed in the VHCF regime were selected for

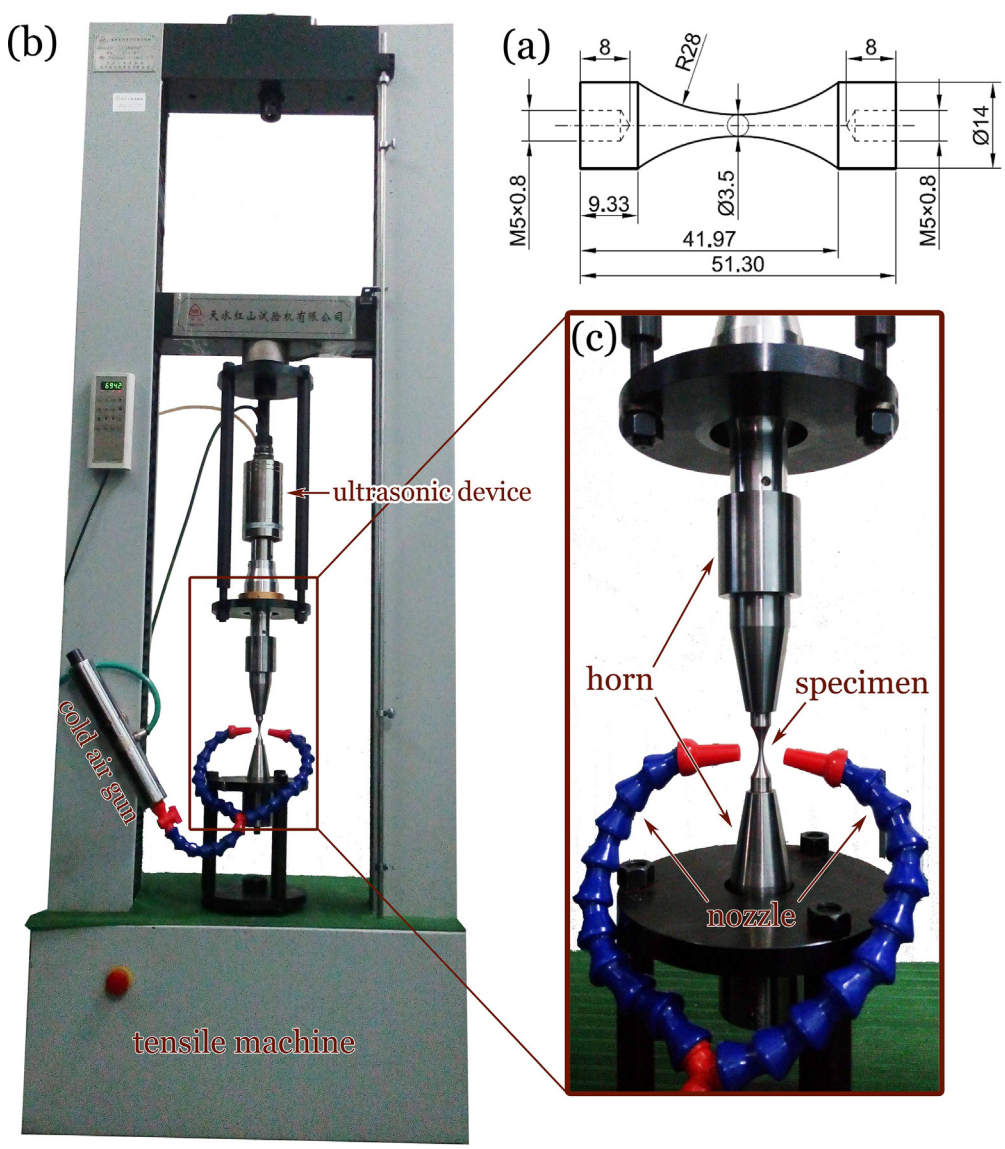

Fig. 2. Ultrasonic fatigue superposed on static tension, (a) geometry of the specimen (dimensions in mm), (b) ultrasonic device connected with a tensile machine, and (c) detail of specimen installation.

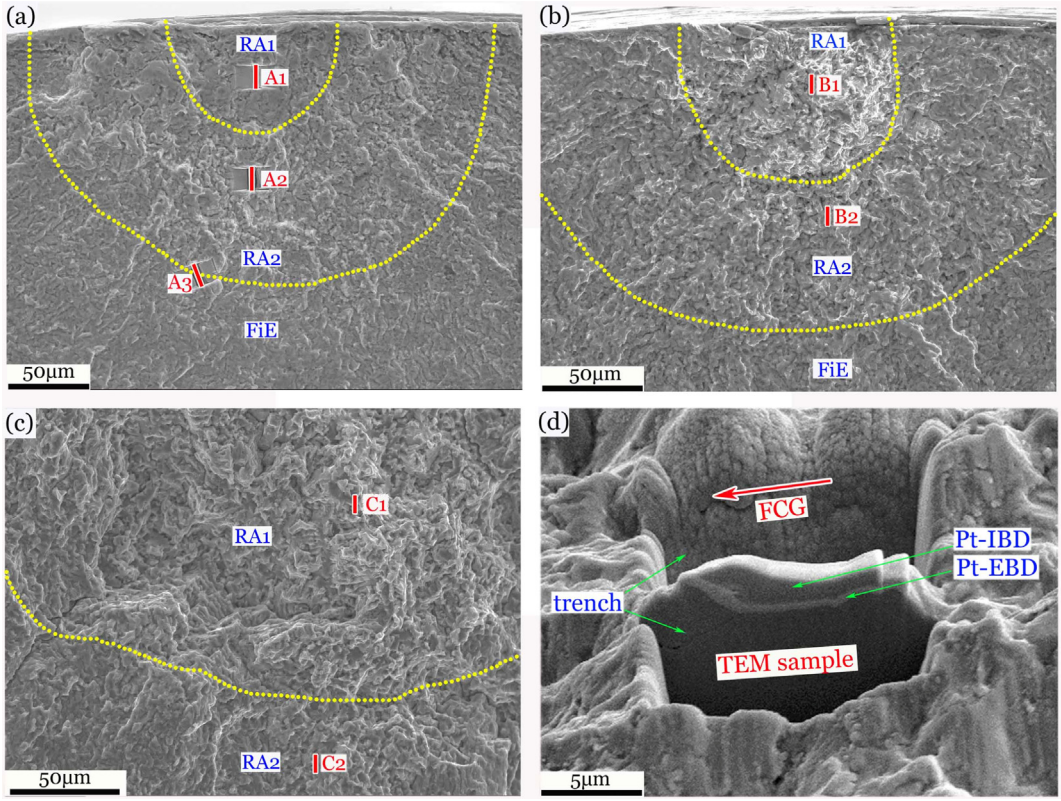

Fig. 3. TEM sample preparation, small bars in (a)-(c) representing TEM sample locations and the red arrow in (d) representing the FCG direction, (a) specimen A: $R = -1$, $\sigma_a = 444$ MPa, and $N_f = 1.508 \times 10^8$, (b) specimen B: $R = 0$, $\sigma_m = 220$ MPa, $\sigma_a = 207$ MPa, and $N_f = 8.633 \times 10^8$, (c) specimen C: $R = 0.5$, $\sigma_m = 440$ MPa, $\sigma_a = 148$ MPa, and $N_f = 1.679 \times 10^8$, and (d) example of FIB milling.

the examination of the fracture surface profile of the crack initiation region. The fatigue failure conditions of these specimens are as follows: specimen A, $\sigma_m = 0$, $R = -1$, $\sigma_a = 444$ MPa, and $N_f = 1.508 \times 10^8$; specimen B, $\sigma_m = 220$ MPa, $R = 0$, $\sigma_a = 207$ MPa, and $N_f = 8.633 \times 10^8$; and specimen C, $\sigma_m = 440$ MPa, $R = 0.5$, $\sigma_a = 148$ MPa, and $N_f = 1.679 \times 10^8$. The TEM samples were cut from these three specimens via the FIB technique equipped in the FEI Helios Nanolab 600i.

Fig. 3a–c shows the locations of the TEM samples from the fatigue crack initiation regions of the specimens. Fig. 3d presents how the TEM sample was cut from the fracture surface via FIB milling. For the protection of the fracture surface, a dual layer of platinum (Pt) coating (Fig. 3d) was deposited on top of the selected location using electrons and Ga^+ in the dual beam FIB system, which was named Pt-EBD (electron beam deposition) and Pt-IBD (ion beam deposition). As a result, seven TEM samples were prepared from specimens A, B and C as shown in Fig. 3a–c: three from specimen A named A1, A2 and A3 (Fig. 3a), two from specimen B named B1 and B2 (Fig. 3b), and two from specimen C named C1 and C2 (Fig. 3c). Each TEM sample is a thin plate with a length of 10 μm, a width of 5 μm and a thickness of 50 nm, which is a perpendicular profile underneath the selected fracture surface.

The TEM samples were carefully examined to obtain the microstructure features underneath the fracture surface of the selected specimens using a JEOL JEM-2100, 2100F and an FEI Tecnai G2 F30 S-Twin. The microstructure morphology of the TEM samples was presented by means of BFI and DFI, and the related electron diffraction was given by SAD. For TEM samples A1-A3, the diameter of the SAD examination was 170 nm, and for other samples, the diameter of the SAD examination was 200 nm.

3. Results and discussion

3.1. Fatigue properties

Fig. 4 shows the fatigue test results in terms of stress amplitude versus mean stress, i.e., the Haigh diagram, with Fig. 4a presenting the fatigue life N_f between 1.2×10^5 and 6.6×10^5 and Fig. 4b presenting N_f between 2.9×10^7 and 1.2×10^9. The Haigh diagram is drawn so that the effect of mean stress on fatigue strength will be readily expressed. For $\sigma_m = 0$, i.e., $R = -1$, the stress amplitude σ_a is between 429 and 533 MPa for the failure cycles N_f between 1.302×10^5 and 6.591×10^5, as shown in Fig. 4a, and the stress amplitude σ_a is between 326 and 503 MPa for the failure cycles N_f between 2.944×10^7 and 1.191×10^9, as shown in Fig. 4b. Then, the average value of the stress amplitudes was defined as σ_{-1} for $\sigma_m = 0$.

Several empirical formulas have been proposed to describe the effect of mean stress on fatigue life [48], among which the Goodman and the Gerber formulas are commonly used. The Goodman relation of Eq. (1) assumes a linear effect of mean stress on fatigue endurance:

$$\frac{\sigma_a}{\sigma_{-1}} = 1 - \frac{\sigma_m}{\sigma_u} \tag{1}$$

where σ_a denotes the stress amplitude, σ_m the mean stress, σ_{-1} the fatigue endurance at $\sigma_m = 0$, and σ_u the UTS. The Gerber relation of Eq. (2) assumes a parabolic effect of mean stress on fatigue endurance:

$$\frac{\sigma_a}{\sigma_{-1}} = 1 - \left(\frac{\sigma_m}{\sigma_u}\right)^2 \tag{2}$$

Then, the average value of σ_{-1} for $\sigma_m = 0$ and the value of UTS σ_u were used to plot the fatigue life curves according to the Goodman and the Gerber relations, as illustrated in Fig. 4. For the HCF regime (Fig. 4a), the Goodman line had relatively good agreement with the test data, and the Gerber curve was less conservative compared to the test

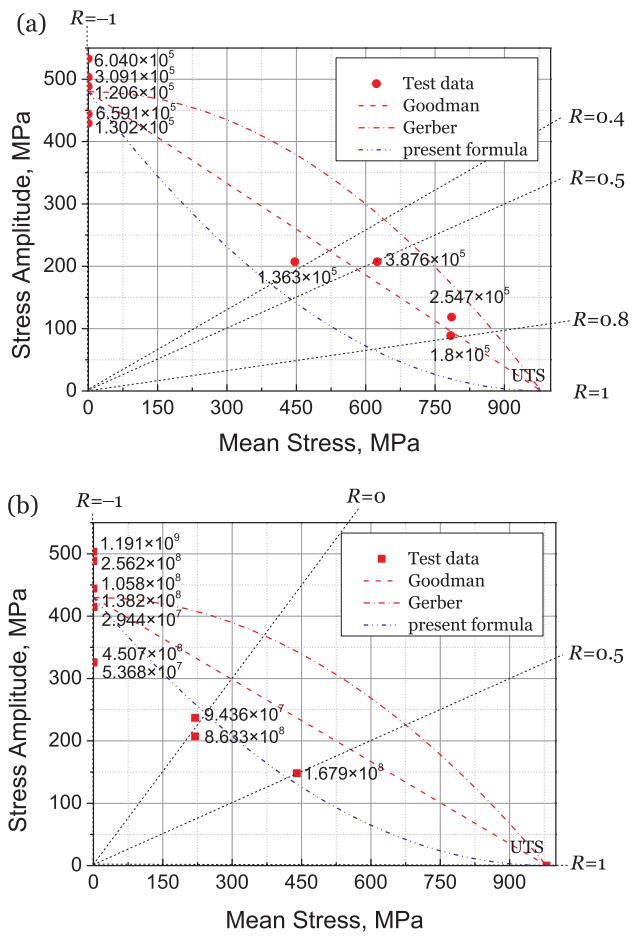

Fig. 4. Haigh diagrams showing fatigue test data, with fatigue failure cycles being labeled for each datum point: (a) for HCF regime and (b) for VHCF regime.

data. For the VHCF regime (Fig. 4b), both the Goodman and the Gerber curves were less conservative compared to the test data.

The Goodman relation considers that the tensile mean stress σ_m linearly weakens the fatigue endurance, as shown in Eq. (1). Obviously, this linear formula underestimates the reduction of fatigue endurance due to the existence of tensile mean stress. Note that σ_{-1} is the fatigue endurance at $\sigma_m = 0$, and it should be related to the strength and ductility of the tested material. Thus, σ_{-1} is considered to be a function of the toughness or consumed energy of the tested material and is written as Eq. (3):

$$\sigma_{-1} = C_1\sigma_u\delta = C_2\frac{\sigma_u^2}{\sigma_y} \tag{3}$$

where C_1 and C_2 are material parameters, δ is the uniform elongation and σ_y is the yield strength of the material. For the cases of $\sigma_m > 0$, σ_a is related to the equivalent toughness, which is uniformly degraded under a given tensile mean stress. Thus, σ_a is expressed as Eq. (4).

$$\sigma_a = C_2\frac{(\sigma_u-\sigma_m)^2}{\sigma_y} \tag{4}$$

By substituting Eqs. (3) into (4), a new formula for σ_a versus σ_m is written as Eq. (5)

$$\sigma_a = \sigma_{-1}\left(1-\frac{\sigma_m}{\sigma_u}\right)^2 \tag{5}$$

The curve of the present formula has a good match to the test data in the VHCF regime, as shown in Fig. 4b, and is relatively conservative in the HCF regime, as shown in Fig. 4a. The different trends of fatigue data in the HCF and VHCF regimes may be ascribed to the transition of the crack initiation mechanism and the failure type due to the existence of tensile mean stress.

3.2. Classification of fatigue crack initiation types

3.2.1. Fatigue failure types

For $\sigma_m = 0$, crack initiation for all specimens was observed from the specimen surface in the HCF and VHCF regimes. For $\sigma_m > 0$, in addition to the crack initiation from the specimen surface, the initiation site may also be in the interior of the specimen in some cases that failed in the VHCF regime.

Three failure types of fracture surface morphology at the location of fatigue crack initiation and early growth were observed and classified. Type I is that cracks initiated at the specimen surface without the RA morphology in the initiation region, as shown in Fig. 5. This failure type occurred in a relatively small part of specimens that failed in the HCF regime for the cases of $\sigma_m = 0$ and $\sigma_m > 0$. This type is named "surface-without-RA".

Type II is that cracks initiated at the specimen surface with the RA morphology at the initiation region, as shown in Fig. 6. This failure type occurred in most specimens that failed in the HCF and VHCF regimes for the cases of $\sigma_m = 0$ and $\sigma_m > 0$. This type is named "surface-with-RA".

Type III is that cracks initiated in the interior or subsurface of specimens with the RA morphology at the initiation region, as shown in

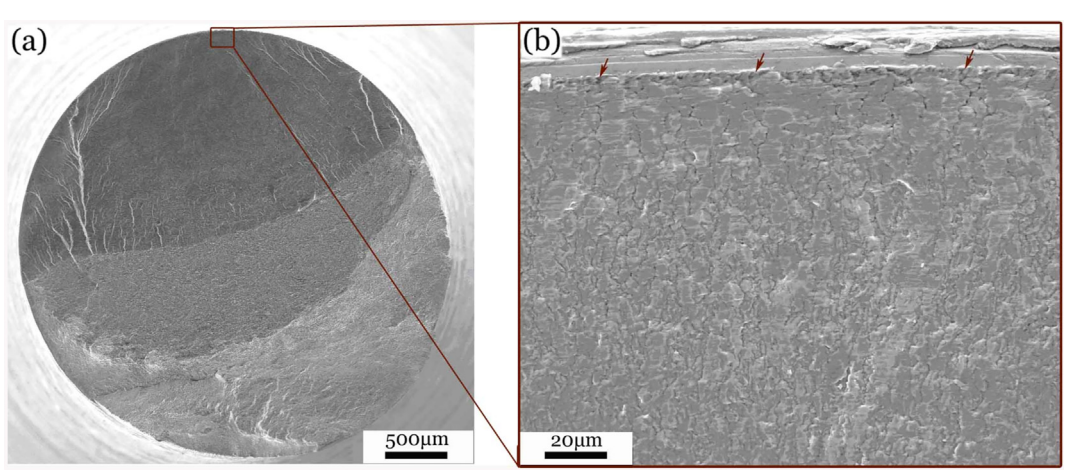

Fig. 5. SEM images of a specimen that failed in HCF regime, $R = -1$, $\sigma_a = 296$ MPa, and $N_f = 6.640 \times 10^6$, showing fractography of surface-without-RA, (a) whole fracture surface and (b) detail for the crack initiation region marked by a box in (a).

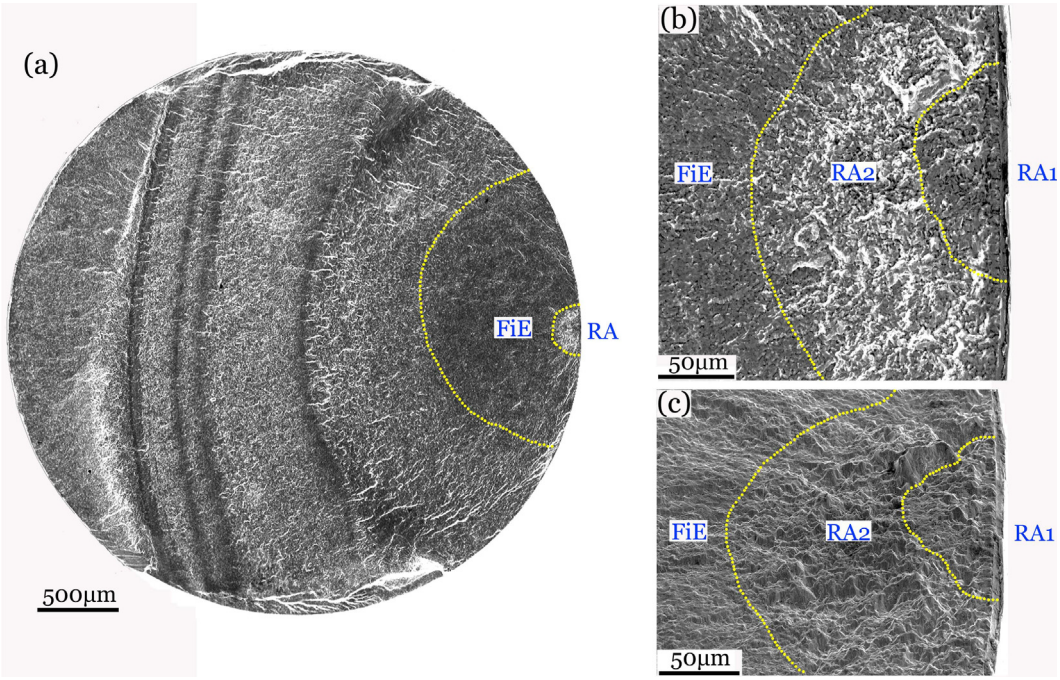

Fig. 6. SEM images of a specimen that failed in HCF regime, $R = -1$, $\sigma_a = 444$ MPa, and $N_f = 7.232 \times 10^6$, showing fractography of surface-with-RA, (a) whole fracture surface, (b) detail for the RA region in (a), and (c) tilted view for the RA region of (b).

Fig. 7. This failure type was observed only in the VHCF regime with $\sigma_m > 0$. This type is named "interior-with-RA".

3.2.2. Crack initiation type of surface-without-RA

Fatigue crack initiation at the specimen surface due to persistent slip bands in LCF and HCF regimes for metallic materials is a common phenomenon [48]. For the case of surface crack initiation, many locations on the surface may have a similar probability of being the fatigue crack initiation site under a given loading condition. In the present case of Fig. 5, fatigue cracks initiated at the surface, but it was difficult to identify the initiation point at the surface even at several different spatial scales (e.g., low magnification for Fig. 5a and high magnification for Fig. 5b). In other words, fatigue cumulative damage did not localize at a specific point of the surface but was evenly distributed over a region along the surface. On the fracture surface, damage pits were observed within the crack initiation region, as shown by the arrows in Fig. 5b. In general, the fatigue crack initiation region exhibited a relatively flat morphology with grinding marks that were more evident in the location close to the specimen surface.

3.2.3. Crack initiation type of surface-with-RA

Different from surface-without-RA, the crack initiation site for surface-with-RA, as shown in Fig. 6, is easily identified on the fracture surface with low magnification SEM, with OM or even by the naked eye. For this failure type, fatigue cracks initiated from the specimen surface, and a localized rough region, i.e., RA, clearly appeared in the crack initiation region. Outside the RA region, an FiE morphology was observed in this failure type, although the FiE morphology did not exhibit an enclosed circular shape like in the case of crack initiation from the interior of the specimen. RA is considered to be the characteristic region of internal crack initiation, and FiE represents the early stage of FCG in VHCF of titanium alloys with BM [3]. In the present case of the titanium alloy with EM, the morphology of RA and FiE still prevails for surface crack initiation in the HCF and VHCF regimes.

It seems that the RA region can be divided into two sub-regions, the inner region RA1 and the outer region RA2, as shown in Fig. 6b and c. Further, there is a gradual transition zone between the RA and FiE regions, which is also seen in Fig. 6c. The failure type of surface-with-RA for the titanium alloy with EM can be described as follows: a crack initiates from the specimen surface and inwardly propagates to form the

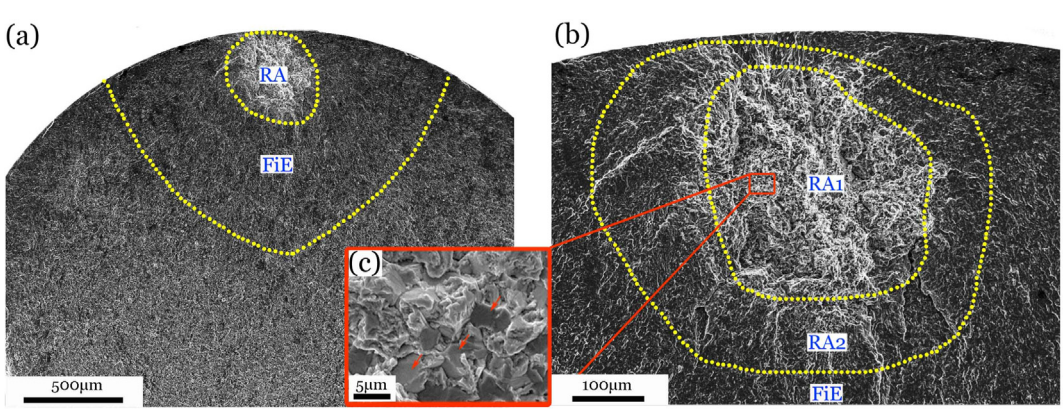

Fig. 7. SEM images of a specimen that failed in VHCF regime, $R = 0.5$, $\sigma_m = 440$ MPa, $\sigma_a = 148$ MPa, and $N_f = 1.679 \times 10^8$, showing the crack initiation type of interior-with-RA, (a) low magnification, (b) high magnification, and (c) cleavage facets.

RA and then FiE region, followed by steady and fast crack growth until final failure in the HCF or VHCF process. This type of morphology demonstrates a typical surface-induced fracture feature, and a similar phenomenon was also observed for high carbon chromium steel [41] in the HCF regime. It is likely that the RA morphology is one of the characteristic fractographic features for surface-induced fatigue damage of metallic materials.

In general, fatigue crack initiation of metallic materials can shift from the specimen surface to the interior with decreasing applied stress in the VHCF regime [45]. However, in the present investigation of the titanium alloy, no crack initiation from the interior or subsurface of specimens was observed in the HCF and VHCF regimes at $\sigma_m = 0$. This can be explained by Chandran's model [49,50]: EGs are regarded as defects evenly distributed in the surface rim and internal area of the titanium alloy with EM, and fatigue crack initiation is more prone to occur from the specimen surface, as a surface defect is more active than an internal defect in causing fatigue crack initiation.

3.2.4. Crack initiation type of interior-with-RA

Fatigue crack initiation in the titanium alloy with EM can shift from the specimen surface to the interior (subsurface) with increasing tensile mean stress. As shown in Fig. 7, crack initiation at the subsurface of specimens with the RA morphology and a vague FiE region was observed, in which fatigue failure occurred in the VHCF regime with $\sigma_m = 440$ MPa ($R = 0.5$). Similarly, the RA region can be divided into two sub-regions, inner RA1 and outer RA2. The RA morphology is clearly presented in Fig. 7a under low magnification, and RA1 and RA2 are also clearly presented in Fig. 7b under high magnification. The RA1 sub-region has a substantial roughness that results from the coalescence of cleavage facets of EGs (shown by the arrows in Fig. 7c). The RA2 sub-region contains many radial ridges in accordance with the FCG direction, and the facet morphology is observed in the region close to its inner boundary.

The typical example in Fig. 8 shows an intermediate state of surface-with-RA shifting to interior-with-RA, for which the specimen failed in the VHCF regime with $\sigma_m = 220$ MPa ($R = 0$) and $N_f = 9.436 \times 10^7$. Fig. 8b shows that the RA1 sub-region is within the specimen subsurface, but the RA2 sub-region intersects the specimen surface.

Based on the observations of Figs. 6–8, it is certain that the RA morphology is a characteristic feature for internal crack-induced VHCF not only in titanium alloys with BM [26,27,32] but also in those with EM, and the crack initiation type of surface-with-RA shifts to interior-with-RA under increasing tensile mean stress, which may degrade the related fatigue endurance.

It should be noted that, in Figs. 6–8, "RA" is the crack initiation region and "FiE" is the crack early growth region after its initiation. In the measurement of FiE size, an FiE envelops its contained RA region, but in the examination of the fracture surface and the profile microstructure, "FiE" is the region outside RA.

3.3. Fracture surface profile morphology and crack initiation mechanism

3.3.1. Case of $R = -1$

Figs. 9–11 show TEM examinations of three locations of the fracture surface profile in the RA region of specimen A (surface-with-RA) that failed in the VHCF regime under $R = -1$.

Fig. 9a presents the TEM image of sample A1 (Fig. 3a) showing the profile of the fracture surface for the microstructure underneath the RA1 region, which contains three layers, Pt-IBD (top black region), the surface layer with vague grain boundaries and the original EM matrix. Fig. 9b–d shows the SAD patterns at the locations just underneath the RA1 surface with discontinuous diffraction rings of polycrystals, which suggests that there are several grains within the SAD area (diameter 170 nm), i.e., nanograins prevail in the selected diffraction area, with a grain size of approximately tens of nanometers. Fig. 9e presents the SAD pattern of elongated diffraction spots, which is the result of texture features due to localized plastic deformation. Fig. 9f and g show typical SAD patterns at locations away from the RA1 surface with isolated spots, which are the normal diffraction patterns of a single crystal, i.e., the original coarse grain of the titanium alloy with EM.

Fig. 10a presents the TEM image of sample A2 (Fig. 3a) showing the profile of the fracture surface for the microstructure underneath the RA2 region, which also contains three layers, Pt-IBD, a gradient layer of microstructure underneath the fracture surface and the original EM with clear grain boundary. Fig. 10b–d shows SAD patterns at the locations just underneath the fracture surface, demonstrating discontinuous rings produced by nanograins. Fig. 10e presents an SAD pattern at a location away from the RA2 surface showing monocrystalline diffraction spots, which implies that the original EM remains. Fig. 10f and g show enlarged DFI for the two dashed boxes that envelope two parts of the gradient layer in Fig. 10a. It is observed that nanograins with the sizes smaller than 50 nm and refined grains with the sizes of approximately 100 nm are successively distributed in the gradient layer perpendicular to the fracture surface underneath the RA2 region.

Fig. 11a presents the TEM image of sample A3 (Fig. 3a) showing the profile of the fracture surface for the microstructure underneath the region between RA and FiE, which mainly contains two layers, Pt-IBD and the original EM with clear grain boundaries. For the SAD detections just underneath the fracture surface, only Fig. 11b from the RA region indicates a polycrystalline feature, but Fig. 11c–e from the FiE region shows monocrystalline diffraction patterns. The SAD detections in Fig. 11f and g away from the fracture surface are also monocrystalline patterns.

This result reveals that nanograin formation together with grain refinement really exists in the RA region during the process of surface

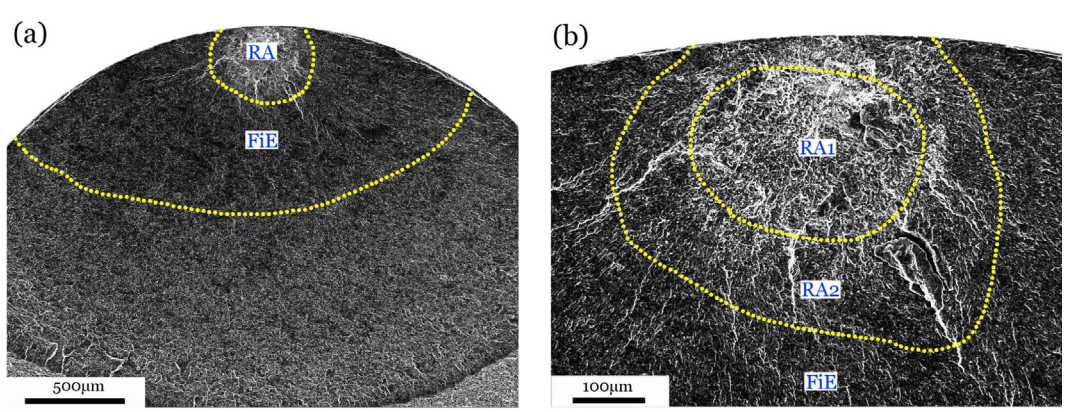

Fig. 8. SEM images of a specimen failed in VHCF regime, $R = 0$, $\sigma_m = 220$ MPa, $\sigma_a = 237$ MPa, and $N_f = 9.436 \times 10^7$, showing crack initiation of interior-with-RA with the RA region intersecting the specimen surface, (a) low magnification and (b) high magnification.

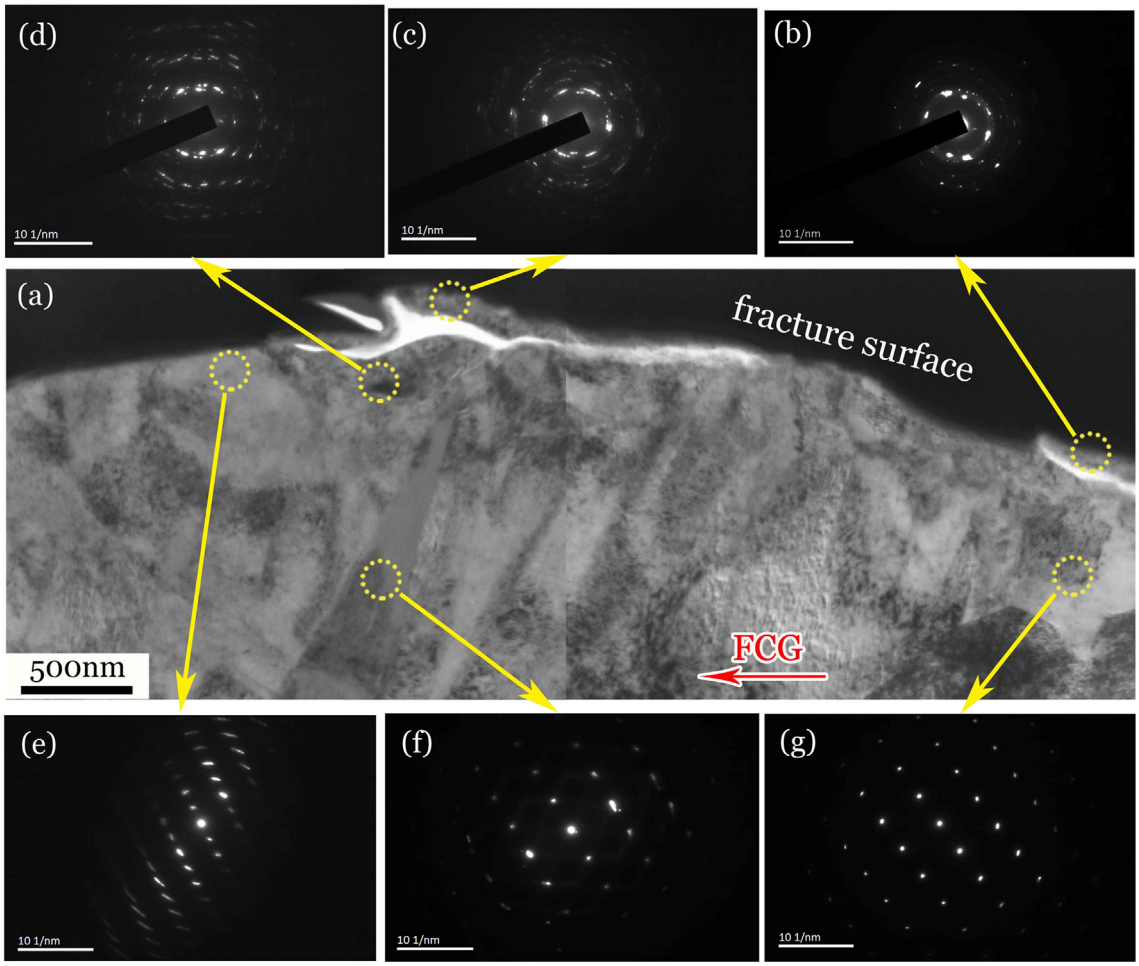

Fig. 9. TEM examinations of sample A1, cut from RA1 of specimen A that failed in VHCF regime, $R = -1$, $\sigma_a = 444$ MPa, and $N_f = 1.508 \times 10^8$, (a) BFI, and (b–g) SAD patterns.

crack initiation-induced VHCF failure of the titanium alloy with EM. This is comparable with the results for the interior crack initiation-induced VHCF failure of the titanium alloy with BM [32] and high-strength steels [31]. For the failure type of surface-with-RA, the process of fatigue crack initiation and early growth is from the specimen surface, which is exposed to the ambient air environment. In other words, the process of nanograin formation and grain refinement in the crack initiation region for the failure type of surface-with-RA means that a vacuum-like environment is not a necessary condition for nanograin formation or grain refinement in the fracture surface layer of the crack initiation region for metallic materials during VHCF, which also supports the NCP model [31].

3.3.2. Cases of $R = 0$ and 0.5

Fig. 12 shows TEM examinations of two locations for the fracture surface profile in the RA region of specimen B (surface-with-RA) that failed in the VHCF regime under $R = 0$.

Fig. 12a presents the TEM image of sample B1 (Fig. 3b) showing the microstructure feature underneath the fracture surface of the RA1 region, which presents the original EM with clear grain boundaries. Fig. 12b presents the TEM image of sample B2 (Fig. 3b) showing the microstructure feature underneath the fracture surface of the RA2 region, which also presents the original EM, and the gray layer on the fracture surface is the Pt-EBD coating. Tens of SAD detections were performed regardless of the location, just underneath or away from the fracture surface within the RA region, and Fig. 12c–j just shows 8 examples of isolated spot patterns indicating only one grain in the diffraction area of 200 nm in diameter. It is suggested that for the case of surface-induced VHCF of the titanium alloy with EM under $R = 0$, the microstructure underneath the fracture surface in the crack initiation region does not undergo grain refinement but maintains the original coarse grains.

Fig. 13 shows TEM examinations of two locations for the fracture surface profile in the RA region of specimen C (interior-with-RA) that failed in the VHCF regime under $R = 0.5$.

Fig. 13a presents the TEM image of sample C1 (Fig. 3c) showing the microstructure feature of the fracture surface underneath the RA1 region, which presents the coarse EG morphology. Fig. 13b presents the TEM image of sample C2 (Fig. 3c) showing the microstructure feature of the fracture surface underneath the RA2 region, which also presents the coarse EG morphology of the original EM. Fig. 13c–j, again, presents examples of tens of SAD detections from different locations of the profile sample, showing diffraction patterns of single crystals that imply no evidence of grain refinement in the RA region in this case. It is evident that for the case of interior crack initiation-induced VHCF of the titanium alloy with EM under $R = 0.5$, the microstructure underneath the fracture surface in the crack initiation region does not undergo grain refinement but maintains the original coarse grains.

It should be emphasized that for specimen B with $R = 0$ and specimen C with $R = 0.5$, the compressive stress is zero, and the tension-tension fatigue mode is applied, for which there is no evidence of nanograin formation underneath the fracture surface in the crack initiation region for VHCF. This is a further revelation in addition to what has been reported for high-strength steels [31] and a titanium alloy with BM [32]. As described in the NCP model by Hong et al. [31], compressive stress is a dominant factor controlling the process of nanograin

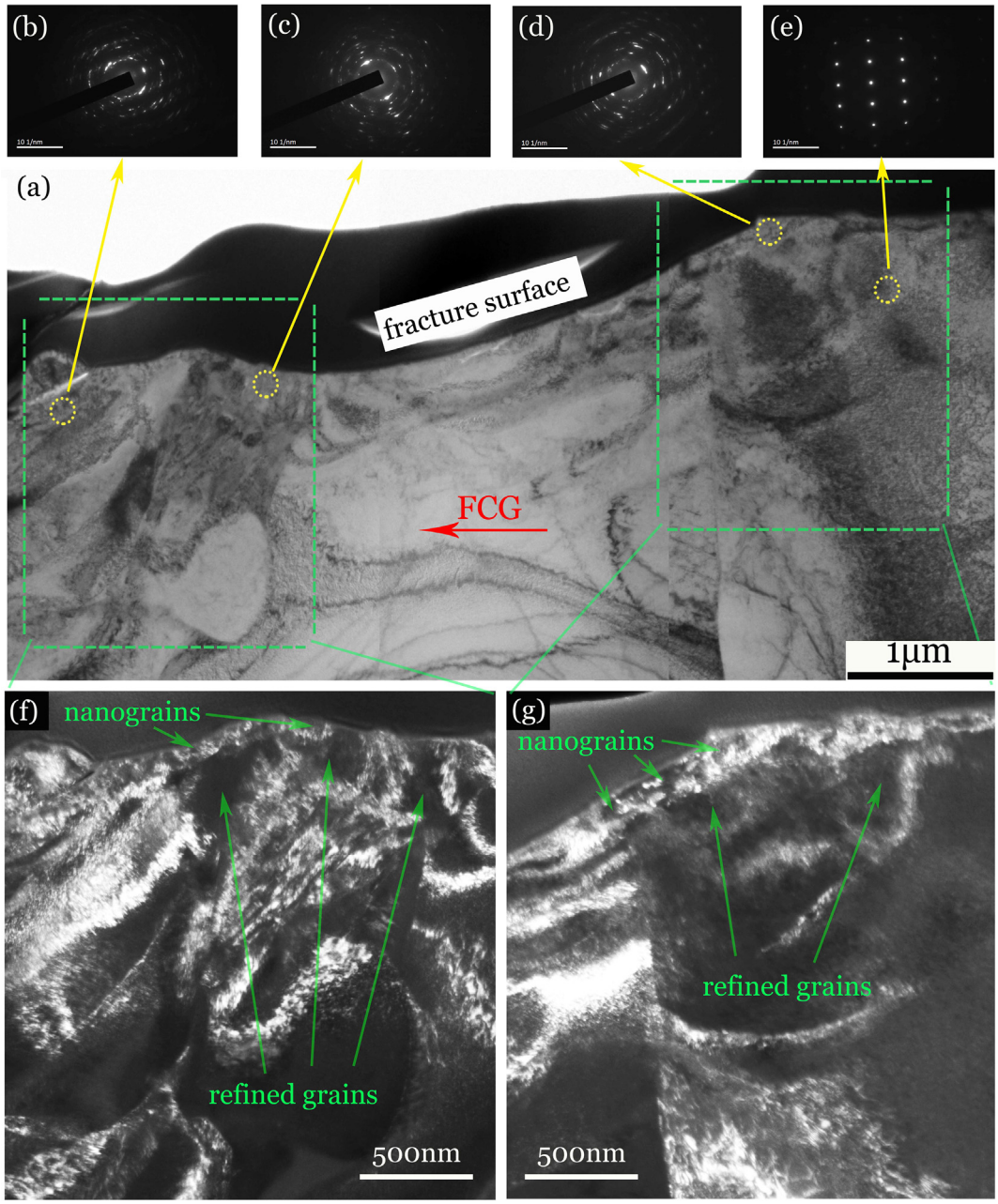

Fig. 10. TEM examinations of sample A2, cut from RA2 of specimen A that failed in VHCF regime, $R = -1$, $\sigma_a = 444$ MPa, and $N_f = 1.508 \times 10^8$, (a) BFI, (b–e) SAD patterns and (f, g) DFI for dashed boxes in (a).

formation, as well as grain size refinement, underneath the fracture surface in the crack initiation region in VHCF of metallic materials. Thus, it is definite that nanograins are less likely to be produced in the crack initiation region for the VHCF process of the tension-tension loading mode. There is a remarkable difference between high-strength steels and titanium alloys: for high-strength steels the FGA morphology diminishes for cases of positive stress ratios, but for titanium alloys the RA morphology prevails regardless of the state of stress ratios; i.e., for some cases ($R \geq 0$), there is no nanograin formation underneath the crack initiation region in the VHCF regime, but the RA morphology may still appear. This can be explained by the fact that for titanium alloys with BM or EM, the RA morphology in the crack initiation region results from the coalescence of cleavage facets, regardless of the loading stress ratio. For the cases of VHCF under a negative stress ratio, the numerous contacting times between the two sides of crack surfaces will cause the formation of nanograins in the RA region, whereas for the case of VHCF under $R \geq 0$, the contacting action between crack surfaces vanishes; thus, the RA region will remain as the original morphology. This revelation for the titanium alloy with EM for $R \geq 0$ together with that from the case for $R = -1$ newly verifies the proposed NCP model [31]. The above revelation with respect to $R \geq 0$ is from the present results of two specimens ($R = 0$ and $R = 0.5$) with EM and one ($R = 0.5$) with BM in Ref. [32]. More specimens of titanium alloys with $R \geq 0$ will be investigated in our future work to further verify this revelation.

4. Conclusions

This paper experimentally investigated the behavior of a TC4 titanium alloy with EM in the HCF and VHCF regimes under different mean stresses. The main conclusions are summarized as follows.

(1) Three types of fatigue crack initiation are observed and classified:

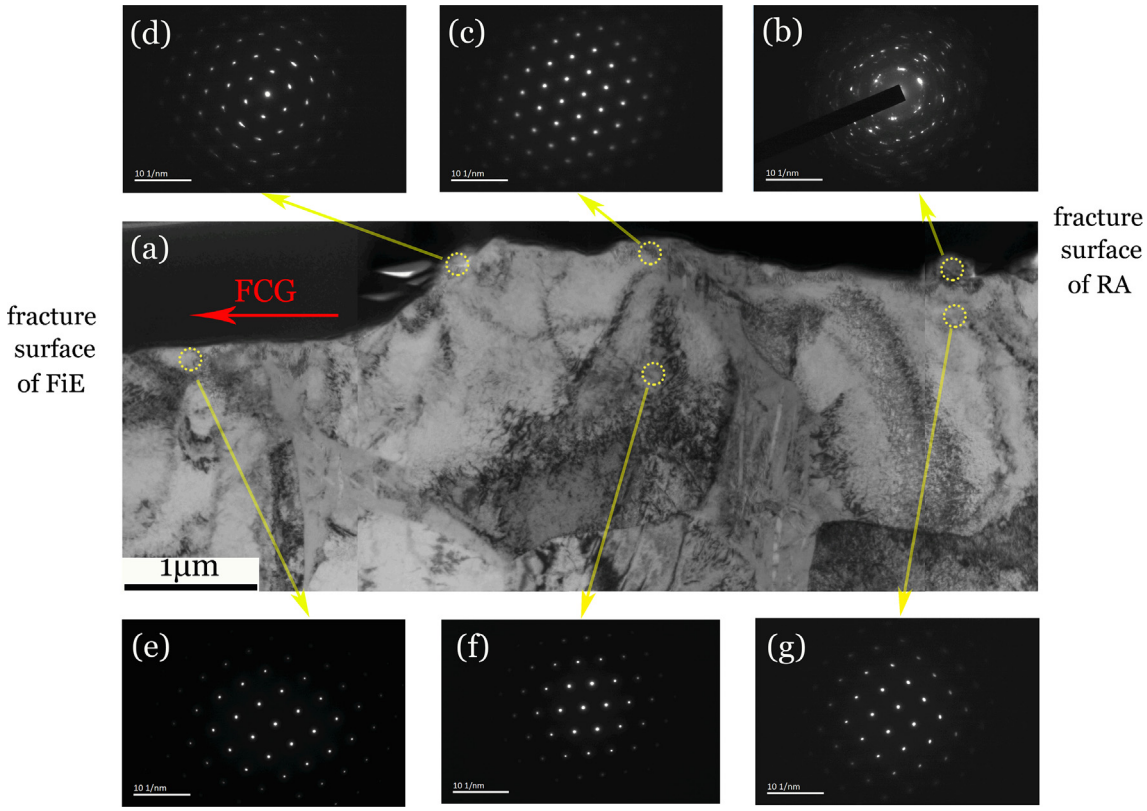

Fig. 11. TEM examinations of sample A3, cut from the region between RA and FiE of specimen A that failed in VHCF regime, $R = -1$, $\sigma_a = 444$ MPa, and $N_f = 1.508 \times 10^8$, (a) BFI, and (b–g) SAD patterns.

crack initiation with surface-without-RA in the HCF regime, surface-with-RA in the HCF and VHCF regimes, and interior-with-RA in the VHCF regime.

(2) Nanograins appear underneath the fracture surface of the RA region only for the cases with negative stress ratios. Nanograin formation in the RA region is a characteristic feature of VHCF, and the formation mechanism is explained by the NCP process.

(3) It is found that nanograin formation exists in the RA region for the

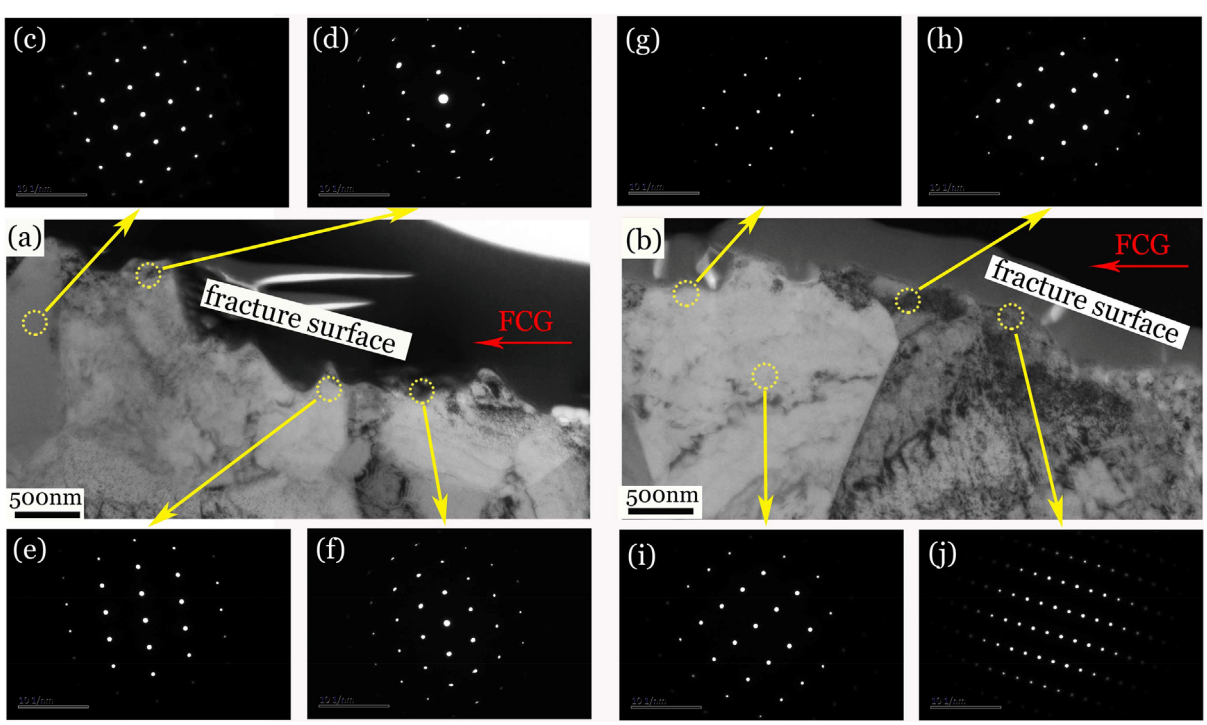

Fig. 12. TEM examinations of specimen B that failed in VHCF regime, $R = 0$, $\sigma_m = 220$ MPa, $\sigma_a = 207$ MPa, and $N_f = 8.633 \times 10^8$, (a) BFI for sample B1 cut from RA1, (b) BFI for sample B2 cut from RA2, and (c–j) SAD patterns.

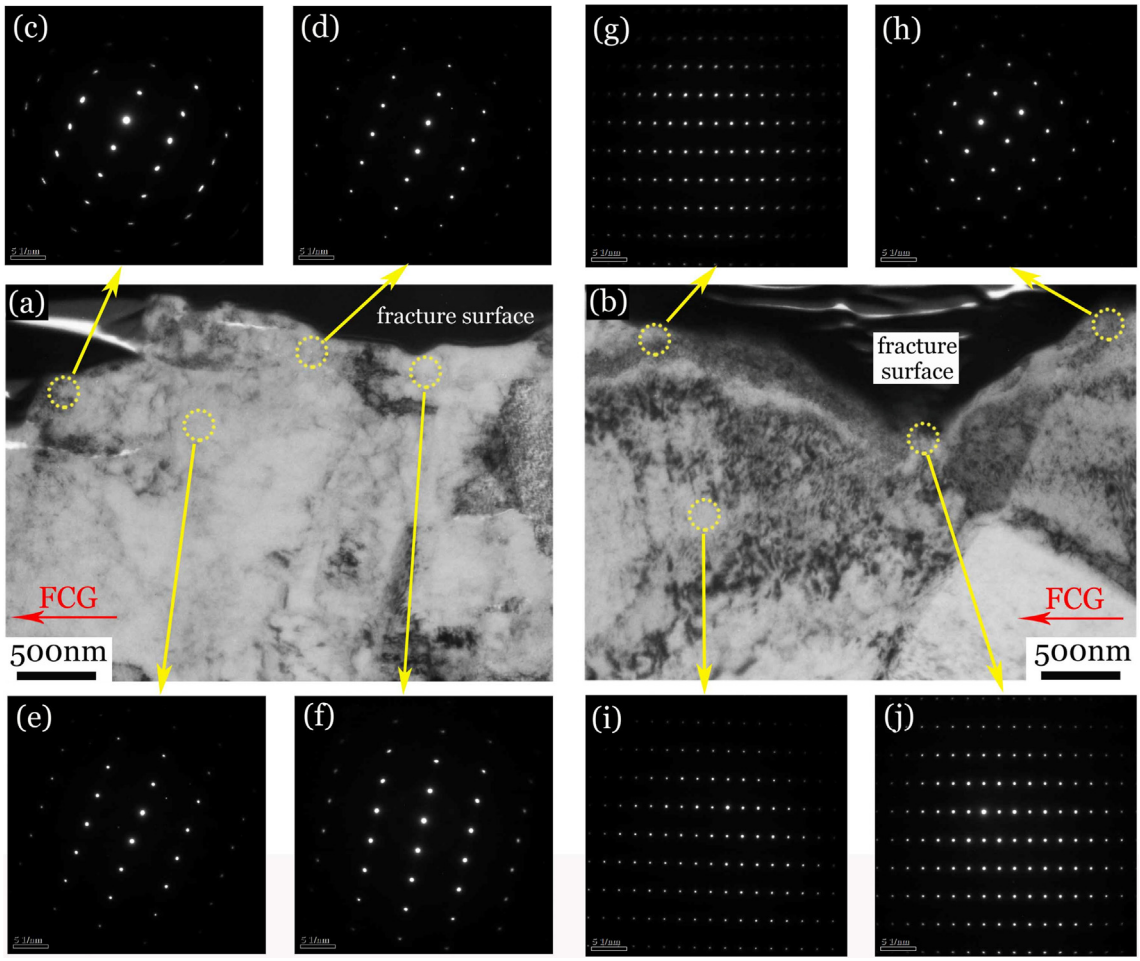

Fig. 13. TEM examinations of specimen C that failed in VHCF regime, $R = 0.5$, $\sigma_m = 440$ MPa, $\sigma_a = 148$ MPa, and $N_f = 1.679 \times 10^8$, (a) BFI for sample C1 cut from RA1, (b) BFI for sample C2 cut from RA2, and (c–j) SAD patterns.

failure type of surface-with-RA in the VHCF regime, suggesting that a vacuum-like environment is not a necessary condition for nano-grain formation in the crack initiation region of VHCF.

Acknowledgments

Financial support from the National Natural Science Foundation of China (11572325) and from the Strategic Priority Research Program of the Chinese Academy of Sciences (XDB22040503, XDB22020201) is greatly acknowledged.

References

[1] Zimmermann M. Diversity of damage evolution during cyclic loading at very high numbers of cycles. Int Mater Rev 2012;57:73–91.
[2] Mayer H. Recent developments in ultrasonic fatigue. Fatigue Fract Eng Mater Struct 2016;39:3–29.
[3] Hong Y, Sun C. The nature and the mechanism of crack initiation and early growth for very-high-cycle fatigue of metallic materials – an overview. Theor Appl Fract Mech 2017;92:331–50.
[4] Pineau A, Forest S. Effects of inclusions on the very high cycle fatigue behaviour of steels. Fatigue Fract Eng Mater Struct 2017;40:1694–707.
[5] Marines-Garcia I, Paris PC, Tada H, Bathias C. Fatigue crack growth from small to long cracks in very-high-cycle fatigue with surface and internal "fish-eye" failures for ferrite-perlitic low carbon steel SAE 8620. Mater Sci Eng A 2007;468–470:120–8.
[6] Hong Y, Lei Z, Sun C, Zhao A. Propensities of crack interior initiation and early growth for very-high-cycle fatigue of high strength steels. Int J Fatigue 2014;58:144–51.
[7] Lei Z, Xie J, Sun C, Hong Y. Effects of loading condition on very-high-cycle fatigue behaviour and dominant variable analysis. Sci China-Phys Mech Astron 2014;57:74–82.
[8] Naito T, Ueda H, Kikuchi M. Observation of fatigue fracture surface of carburized steel. J Soc Mater Sci 1983;32:1162–6.
[9] Naito T, Ueda H, Kikuchi M. Fatigue behavior of carburized steel with internal oxides and nonmartensitic microstructure near the surface. Metall Trans 1984;15A:1431–6.
[10] Atrens A, Hoffelner W, Duerig T, Allison J. Subsurface crack initiation in high cycle fatigue in Ti-6Al-4V and in a typical martensitic stainless steel. Scr Metall 1983;17:601–6.
[11] Nishijima S, Kanazawa K. Stepwise S-N curve and fish-eye failure in gigacycle fatigue. Fatigue Fract Eng Mater Struct 1999;22:601–7.
[12] Sakai T, Takeda M, Shiozawa K, Ochi Y, Nakajima M, Nakamura T, et al. Experimental reconfirmation of characteristic S-N property for high carbon chromium bearing steel in wide life region in rotating bending. J Soc Mater Sci 2000;49:779–85.
[13] Grad P, Kerscher E. Reason for the transition of fatigue crack initiation site from surface to subsurface inclusions in high-strength steels. Fatigue Fract Eng Mater Struct 2017;40:1718–30.
[14] Spriestersbach D, Grad P, Kerscher E. Threshold values for very high cycle fatigue failure of high-strength steels. Fatigue Fract Eng Mater Struct 2017;40:1708–17.
[15] Murakami Y. Metal fatigue: effect of small defects and nonmetallic inclusions. Oxford: Elsevier; 2002.
[16] Stanzl-Tschegg S, Schönbauer B. Near-threshold fatigue crack propagation and internal cracks in steel. Procedia Eng 2010;2:1547–55.
[17] Stanzl-Tschegg S. Fracture mechanical characterization of the initiation and growth of interior fatigue cracks. Fatigue Fract Eng Mater Struct 2017;40:1741–51.
[18] Zhao A, Xie J, Sun C, Lei Z, Hong Y. Prediction of threshold value for FGA formation. Mater Sci Eng A 2011;528:6872–7.
[19] Wu G, Shi C, Sha W, Sha A, Jiang H. Effect of microstructure on the fatigue properties of Ti-6Al-4V titanium alloys. Int J Fatigue 2013;46:668–74.
[20] Neal F, Blenkinsop P. Internal fatigue origins in α-β titanium alloys. Acta Metall 1976;24:59–63.
[21] Huang Z, Liu H, Wang C, Wang Q. Fatigue life dispersion and thermal dissipation investigations for titanium alloy TC17 in very high cycle regime. Fatigue Fract Eng Mater Struct 2015;38:1285–93.
[22] Zuo J, Wang Z, Han E. Effect of microstructure on ultra-high cycle fatigue behavior of Ti-6Al-4V. Mater Sci Eng A 2008;473:147–52.

[23] Liu X, Sun C, Hong Y. Effects of stress ratio on high-cycle and very-high-cycle fatigue behavior of a Ti-6Al-4V alloy. Mater Sci Eng A 2015;622:228–35.
[24] Liu X, Sun C, Hong Y. Faceted crack initiation characteristics for high-cycle and very-high-cycle fatigue of a titanium alloy under different stress ratios. Int J Fatigue 2016;92:434–41.
[25] Heinz S, Balle F, Wagner G, Eifler D. Analysis of fatigue properties and failure mechanisms of Ti6Al4V in the very high cycle fatigue regime using ultrasonic technology and 3D laser scanning vibrometry. Ultrasonics 2013;53:1433–40.
[26] Heinz S, Eifler D. Crack initiation mechanisms of Ti6Al4V in the very high cycle fatigue regime. Int J Fatigue 2016;93:301–8.
[27] Takeuchi E, Furuya Y, Nagashima N, Matsuoka S. The effect of frequency on the giga-cycle fatigue properties of a Ti-6Al-4V alloy. Fatigue Fract Eng Mater Struct 2008;31:599–605.
[28] Furuya Y, Takeuchi E. Gigacycle fatigue properties of Ti–6Al–4V alloy under tensile mean stress. Mater Sci Eng A 2014;598:135–40.
[29] Oguma H, Nakamura T. The effect of microstructure on very high cycle fatigue properties in Ti-6Al-4V. Scr Mater 2010;63:32–4.
[30] Oguma H, Nakamura T. Fatigue crack propagation properties of Ti-6Al-4V in vacuum environments. Int J Fatigue 2013;50:89–93.
[31] Hong Y, Liu X, Lei Z, Sun C. The formation mechanism of characteristic region at crack initiation for very-high-cycle fatigue of high-strength steels. Int J Fatigue 2016;89:108–18.
[32] Su H, Liu X, Sun C, Hong Y. Nanograin layer formation at crack initiation region for very-high-cycle fatigue of a Ti-6Al-4V alloy. Fatigue Fract Eng Mater Struct 2017;40:979–93.
[33] Ritchie R, Davidson D, Boyce B, Campbell J, Roder O. High-cycle fatigue of Ti-6Al-4V. Fatigue Fract Eng Mater Struct 1999;22:621–31.
[34] Sadananda K, Vasudevan A. Fatigue crack growth behavior of titanium alloys. Int J Fatigue 2005;27:1255–66.
[35] Lee E, Vasudevan A, Sadananda K. Effects of various environments on fatigue crack growth in Laser formed and IM Ti–6Al–4V alloys. Int J Fatigue 2005;27:1597–607.
[36] Petit J, Sarrazin-Baudoux C. An overview on the influence of the atmosphere environment on ultra-high-cycle fatigue and ultra-slow fatigue crack propagation. Int J Fatigue 2006;28:1471–8.
[37] McEvily A, Nakamura T, Oguma H, Yamashita K, Matsunaga H, Endo M. On the mechanism of very high cycle fatigue in Ti-6Al-4V. Scr Mater 2008;59:1207–9.
[38] Sarrazin-Baudoux C, Stanzl-Tschegg S, Schönbauer B, Petit J. Ultra-slow fatigue crack propagation in metallic alloys. Procedia Eng 2016;160:151–7.
[39] Spriestersbach D, Brodyanski A, Lösch J, Kopnarski M, Kerscher E. Very high cycle fatigue of bearing steels with artificial defects in vacuum. Mater Sci Tech 2016;32:1111–8.
[40] Spriestersbach D, Brodyanski A, Lösch J, Kopnarski M, Kerscher E. Very high cycle fatigue of high-strength steels: crack initiation by FGA formation investigated at artificial defects. Procedia Struct Integrity 2016;2:1101–8.
[41] Sakai T, Sato Y, Nagano Y, Takeda M, Oguma N. Effect of stress ratio on long life fatigue behavior of high carbon chromium bearing steel under axial loading. Int J Fatigue 2006;28:1547–54.
[42] Cao F, Chandran K. The role of crack origin size and early stage crack growth on high cycle fatigue of powder metallurgy Ti-6Al-4V alloy. Int J Fatigue 2017;102:48–58.
[43] Sun C, Lei Z, Hong Y. Effects of stress ratio on crack growth rate and fatigue strength for high cycle and very-high-cycle fatigue of metallic materials. Mech Mater 2014;69:227–36.
[44] Chandran K. A new approach to the mechanics of fatigue crack growth in metals: correlation of mean stress (stress ratio) effects using the change in net-section strain energy. Acta Mater 2017;135:201–14.
[45] Bathias C, Paris P. Gigacycle fatigue in mechanical practice. New York: Marcel Dekker; 2005.
[46] Bathias C. Piezoelectric fatigue testing machines and devices. Int J Fatigue 2006;28:1438–45.
[47] Nikitin A, Bathias C, Palin-Luc T. A new piezoelectric fatigue testing machine in pure torsion for ultrasonic gigacycle fatigue tests: application to forged and extruded titanium alloys. Fatigue Fract Eng Mater Struct 2015;38:1294–304.
[48] Suresh S. Fatigue of materials. 2nd ed. Cambridge University Press; 1998.
[49] Chandran K. Duality of fatigue failures of materials caused by Poisson defect statistics of competing failure modes. Nat Mater 2005;4:303–8.
[50] Chandran K, Jha S. Duality of the S-N fatigue curve caused by competing failure modes in a titanium alloy and the role of Poisson defect statistics. Acta Mater 2005;53:1867–81.